Multi-physical fields distribution in billet during helical electromagnetic stirring: A numerical simulation research

*Dong Pan[1, 2], Qing-tao Guo[1, 2], Kai-lun Zhang[1, 2], Fu-zhi Yu[1, 2], Yu-ying Li[1, 2], and Yu-bao Xiao[1, 2]

1. State Key Laboratory of Metal Materials for Marine Equipment and Application, Anshan 114009, Liaoning, China

2. Ansteel Beijing Research Institute Co., Ltd., Beijing 102200, China

Abstract: Electromagnetic stirring is one of the widely applied techniques to modify the quality of casting billets. Different from conventional rotate stirring, the helical stirring is more professional in assisting multi-dimensional flow of molten metal and eliminating solidification defects. In this study, the single-winding helical stirring (SWHS) was introduced, offering advantages such as smaller volume and lower electromagnetic shielding compared to traditional helical stirring methods. Following a comprehensive numerical simulation, the stirring parameters of SWHS were adjusted to yoke inclination angle of 43° and frequency of 12 Hz. The higher electromagnetic force and flow velocity in drawing direction, as well as the lower temperature gradient induced by the SWHS, are positive factors for homogeneous solidification of billet. The experimental results on Al-8%Si alloy and 0.4%C-1.1%Mn steel demonstrate that compared to rotate stirring, the SWHS process can induce better billet quality and is more effective in accelerating the equiaxed expansion and reducing element segregation. The SWHS process can enhance the equiaxed ratio of the billet by 58.3% and reduce segregation degree of carbon element by 10.97%. Consequently, SWHS holds great promise as a potential approach for improving the quality of continuous casting billets.

Keywords: billet; electromagnetic stirring; helical; solidification; element segregation; numerical simulation

CLC numbers: TP391.9   Document code: A   Article ID: 1672-6421(2024)01-051-09

1 Introduction

The mass transfer and heat transfer in molten steel which can be affected by external electromagnetic field during solidification have a vital influence on the quality of billet [1-3]. In recent years, with the development of electromagnetic metallurgy technology [4, 5], the electromagnetic stirring has been widely applied due to its advantages in increasing the equiaxed grain rate, decreasing shrinkage porosity, and reducing solute element segregation [6]. Generally, the type of electromagnetic stirring is classified into rotary stirring, traveling wave stirring, and helical stirring. Compared with the other two stirring methods, the helical stirring plays a more important role in accelerating the mass and heat transfer in three-dimension direction [7]. Zhao et al. [8] confirmed that the density segregation of Sn-11Sb ingot can be lightened by helical stirring. Therefore, the helical stirring has attracted widespread attention and become a hot research spot.

In 1980s, French scholar invented the helical stirrer suitable for secondary cooling zone of continuous casting billet [9]. It was composed of a group of traveling wave sensors and rotating sensors. However, this kind of stirrer has an excessive volume, so that it has not been adopted. Our previous research [10] has demonstrated that the helical stirring of molten metal can be realized by using one set of coils with special structure of the magnetic yoke. Through this single-winding helical stirring (SWHS), the internal quality of bloom can be significantly improved [10]. However, rare attention has been paid to its application in billet due to the limited volume fraction of liquid cave at the end of secondary cooling zone of a billet. Meanwhile, according to Bridge's study [11], inappropriate stirring parameters will lead to the formation of white belt. Therefore, it is of significant to explore the heat and mass transfer of helical stirring of billet.

*Dong Pan

Born in Linyi, Shandong, Ph. D. His research interests primarily focus on thermal simulation of solidification structure of continuous casting billets, electromagnetic stirring of liquid metals, electroinduced toughening of solid metals, and development of special steel products. To date, he has published over 20 papers in SCI, EI and CA index journals, and held three invention patents of China.

E-mail: agbjyPD@163.com

In this work, to investigate the feasibility of helical electromagnetic stirring for continuous casting billet, numerical simulation on physical fields was conducted. In addition to helical stirring, research on rotary stirring was also conducted to further highlight the improved stirring effect of SWHS. To further verify the universality of helical electromagnetic stirring in improving the quality of various metal billets, the Al-8.8Si alloy and 0.4%C-1.1%Mn steel were used for solidification stirring experiment, aiming to provide a theoretical basis and technical reference for the application of SWHS in billet production.

2 Numerical simulation

Firstly, the multi-physical field equations involved in the numerical simulation of electromagnetic stirring need to be confirmed. The electromagnetic force ($\vec{F}$, N) was calculated based on the Maxwell equation [12]:

$$\vec{F} = \frac{1}{\mu}(\nabla \cdot \vec{B})\vec{B} - \nabla\left(\frac{\vec{B}^2}{2\mu}\right) \tag{1}$$

where $\vec{B}$ represents the magnetic flux intensity (T), and μ is magnetoconductivity (H·m^{-1}). The flow field is governed by Navier-Stokes equation [13]:

$$\frac{\partial(\rho\vec{u})}{\partial t} + (\rho\vec{u}\cdot\nabla)\vec{u} = -\nabla p + \eta_{\text{eff}}\nabla^2\vec{u} + \rho g + \vec{F} \tag{2}$$

where $\vec{u}$ is flow velocity (m·s^{-1}), ρ refers to density (kg·m^{-3}), g is gravitational acceleration, $\vec{F}$ means the electromagnetic force, and the η_{eff} is effective viscosity (kg·m^{-1}·s^{-1}). The effective viscosity is the sum of dynamic viscosity (η) and

turbulent viscosity (η_t) [13]:

$$\begin{cases} \eta_{\text{eff}} = \eta + \eta_t \\ \eta_t = \rho C_u \dfrac{k^2}{\varepsilon} \end{cases} \tag{3}$$

where C_u is empirical constant, k is the turbulent kinetic energy, and ε is the dissipation rate of turbulent kinetic energy. The mass conservation equation is [13]:

$$\frac{\partial\rho}{\partial t} + \nabla\cdot(\rho\vec{u}) = 0 \tag{4}$$

where t is the time. The heat conservation equation is governed by [13]:

$$Q = \rho C_p \frac{\partial T}{\partial t} - \nabla\cdot k_h\nabla T \tag{5}$$

where Q is the heat generated by the Joule heating effect, k_h is the thermal conductivity, T is the temperature, and C_p is the specific heat.

The model of electromagnetic stirrer is shown in Fig. 1. The electromagnetic stirring force generated between adjacent yokes in rotate stirrer is perpendicular to the coil planes, as shown in Fig. 1(d). By tilting the yoke at a certain angle (θ), the electromagnetic force can be divided into horizontal circumferential force (F_R) and force along the drawing direction (F_T). In this way, the SWHS for continuous casting billet was constructed [Fig. 1(c)]. The stirrer model for numerical simulation is given in Figs. 1(a) and (b). The internal diameter and external diameter of the stirrer were 200 mm and 323 mm, respectively. The interval gap between adjacent yokes was 20 mm, and the height of the stirrer was 200 mm. The length of billet was 2 m, and the section size of the billet measured
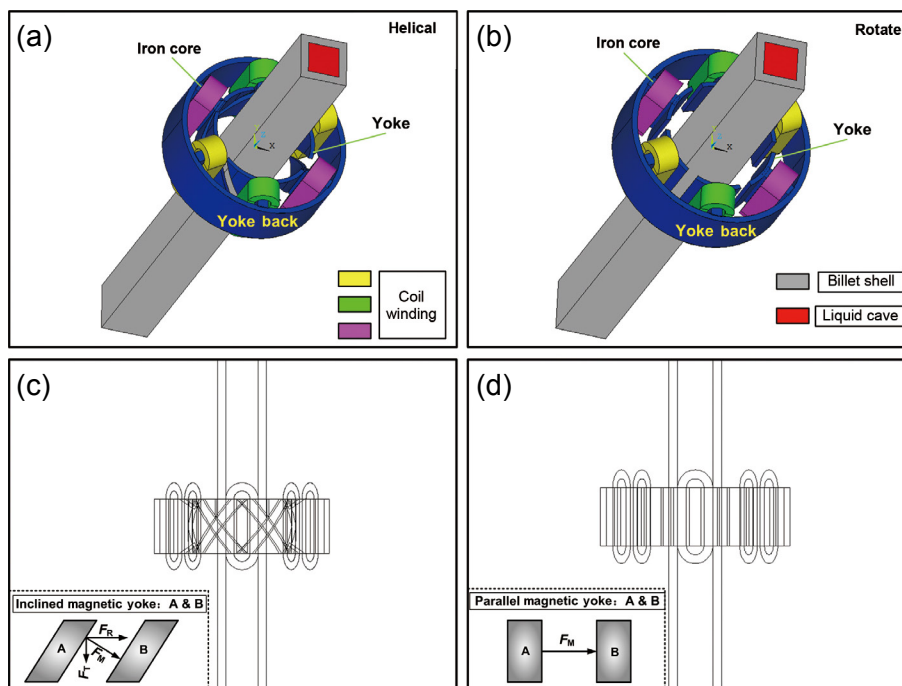

Fig. 1: Electromagnetic stirrer's model: (a) helical stirrer; (b) rotate stirrer; (c) front view of helical stirrer; (d) front view of rotate stirrer (F_M is electromagnetic stirring force; F_R is circumferential component force of F_M; F_T is component force of F_M along drawing direction)

200 mm×200 mm and the liquid cave located at the center of billet measured 120 mm×120 mm.

The excitation current was set to 3×10^6 A. The frequency was in the range of 2 Hz–12 Hz, the yoke inclination angle (θ) was between 35°–45°, and the phase difference of current between adjacent yokes was 120°. Regarding the boundary condition setting for flow field simulation, the initial temperature of the liquid core was set to 1,490 °C (superheat: 30 °C). The two sections of the billet were designated as the inlet and outlet, while other planes were assigned as walls. The material used in numerical simulation was 0.4%C-1.1%Mn steel, and its thermophysical parameters were listed in Table 1.

Table 1: Thermophysical parameters of the 0.4%C-1.1%Mn steel used in simulation

Parameter	Density (ρ, kg·m^{-3})	Specific heat (C_p, J·kg^{-1}·K^{-1})	Thermal conductivity (k_h, W·m^{-1}·K^{-1})	Viscosity (η_{eff}, kg·m^{-1}·s^{-1})
Value	7,020	680	34	6.2×10^{-3}

3 Experimental procedure

The Al-8.8Si alloy (chemical composition: 8.8wt.%Si, balance Al) and 0.4%C-1.1%Mn steel (chemical composition: 0.40wt.% C, 1.10wt.% Mn, balance Fe) were used as experimental materials to examine the effect of helical stirring and rotate stirring. The Al-8.8Si alloy was placed in an alumina crucible and heated at 780 °C for 15 min to ensure complete melting. Then, the crucible, after slowly cooled to 680 °C, was placed in the electromagnetic stirring device for helical and rotate stirring, until the Al-8.8Si alloy was totally solidified. For 0.4%C-1.1%Mn steel, it was melted at 1,520 °C for 30 min, then, cooled to 1,490 °C for helical and rotate stirring until complete solidification. The yoke inclination angle for helical stirring was 43° and the frequency was 12 Hz. The current for the stirring of Al-8.8Si alloy and 0.4%C-1.1%Mn steel was 75 A and 300 A, respectively. Finally, the cylindrical ingots (Φ130 mm×200 mm) were obtained.

The element segregation and solidification structure were characterized to measure the stirring effect [10]. The 0.4%C-1.1%Mn steel sample was etched by a 4% (volume fraction) nitrate alcohol mixed solution and the Al-8.8Si sample was etched by Keller's reagent (2.5% nitric acid + 1% hydrochloric acid + 1% hydrofluoric acid + 95.5% water) both for about 15 s at room temperature. The etched samples were used for structure observation. An electric spark in-situ analyzer (SparkCCD 7000 type) was adopted for detection of element segregation degree of 0.4%C-1.1%Mn steel. The confidence level of this statistical method is 95%. For the Al-8.8Si alloy, ICP test of the drilled chips at the upper, middle, and lower points on the center line of the longitudinal section of the billet was conducted using a Plasma 3000 tester to measure the distribution of Si content.

4 Results and discussion

4.1 Optimization of helical stirrer's structure and current frequency

The optimization of the structure and frequency of the helical stirrer was based on sufficient electromagnetic force along the drawing direction. In this section, the effect of current frequency and yoke inclination on F_T was discussed. At first, the effect of frequency on electromagnetic force was calculated, as the yoke inclination remains consistent. As depicted in Fig. 2, the region with higher electromagnetic force F_T is mainly distributed within the range of about 0.5 m to 1.0 m along the drawing direction. Besides, with the increment in frequency, the maximum value of F_T increases before the frequency reaches 12 Hz. Whereas, as the frequency exceeds 12 Hz, the value of F_T begins to decrease. The relationship between frequency (f), the electromagnetic force considering skin effect ($\vec{F}_s$), and the distance from the surface of the melt (l) was governed by [14]:

$$\left\{ \begin{array}{c} \vec{F}_s = \sqrt{\dfrac{\pi f \sigma}{\mu}} \cdot B_0^2 \, \exp\left(-\dfrac{2l}{x}\right) \\ x = 1/\sqrt{\pi f \mu \sigma} \end{array} \right\} \qquad (6)$$

where B_0 means magnetic induction intensity, σ is conductivity,
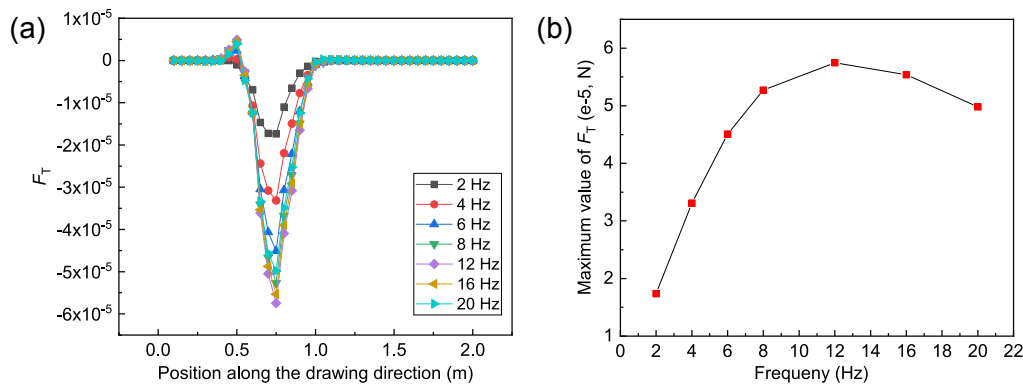

Fig. 2: Effect of current frequency on electromagnetic force along the drawing direction: (a) distribution curves of F_T along the drawing direction; (b) relationship between maximum value of F_T and frequency

μ refers to permeability, and x represents the skin depth. According to Eq. (6), the relationship between $\vec{F}_S$ and f is not monotonic. At lower frequencies, an increase in frequency leads to a gradual increase in the electromagnetic force. However, when the frequency reaches a certain value, the skin effect becomes significant and the electromagnetic force in the billet starts to decrease. As a result, the value of $\vec{F}_S$ will increase at first and then decrease with the increase of f. Therefore, the optimized frequency for helical stirring is 12 Hz.

The effect of yoke inclination angle (θ) on electromagnetic force is demonstrated in Fig. 3. The relationship between F_T and F_M is: $F_T=F_M\times\sin\theta$, so the value of F_T initially shows a gradual increase with the increase of θ, as shown in Fig. 3(b). However, as the θ of the yoke increases, the distance (d) from the tip of the yoke to the coil increases, which leads to a decrease in the magnetic conductivity of the yoke and F_T [10]. From the results shown in Fig. 3(b), it can be observed that when the value of θ exceeds 43°, the field transmission (F_T) starts to decrease due to an excessive distance between yoke tips and coils. Therefore, the optimized parameters for numerical simulation of SWHS are 12 Hz and 43°, respectively.

4.2 Comparison between rotate stirring and helical stirring

Figure 4 shows the vector distribution of F_M. It indicates that the direction of F_M vector is parallel to the radial direction of rotate stirrer, whereas in helical stirrer, the F_M tends to distribute along the drawing direction. As shown in Figs. 4(c) and (d), the distribution of the F_M contour in helical stirrer is more homogeneous than that in rotate stirrer. Besides, the area with higher F_M distributed around the center of cross section of helical stirrer is also larger. Moreover, based on the results of Fig. 5, the value of F_T in helical stirring is obviously higher than the rotate stirring. This implies that compared with rotate stirrer, the molten steel can be stirred more thoroughly in helical stirrer.
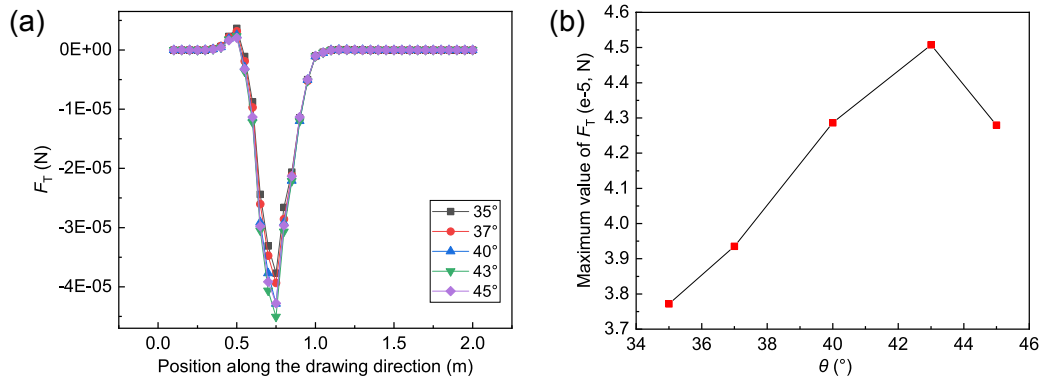

Fig. 3: Effect of yoke inclination angle (θ) on electromagnetic force: (a) distribution curves of F_T along the drawing direction; (b) relationship between maximum value of F_T and θ
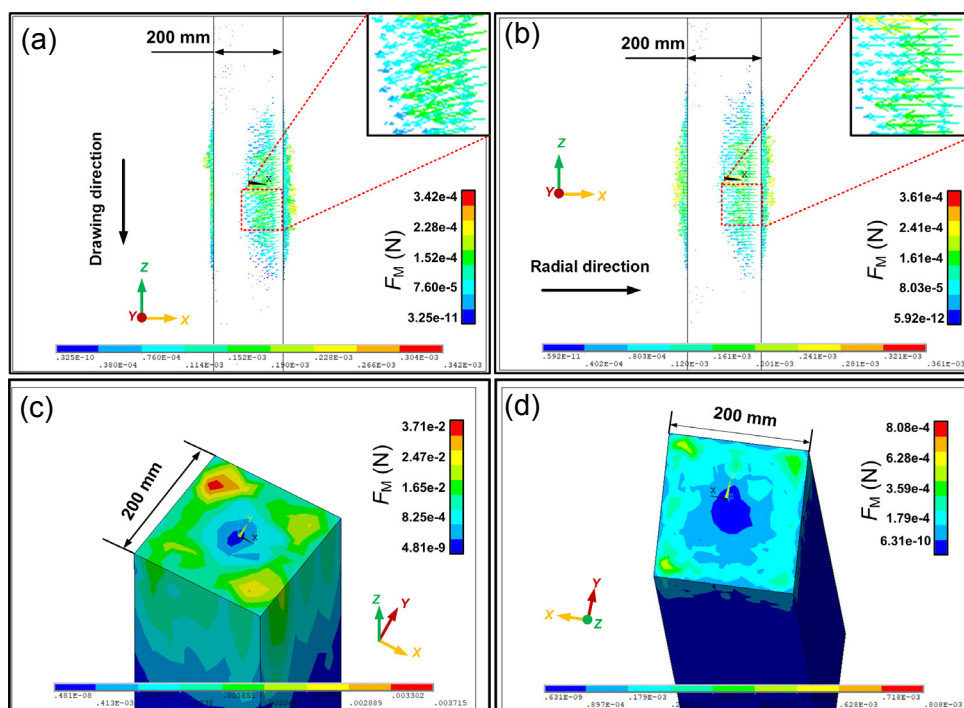

Fig. 4: Vector and contour distribution of electromagnetic force of helical (a, c) and rotate stirring (b, d)
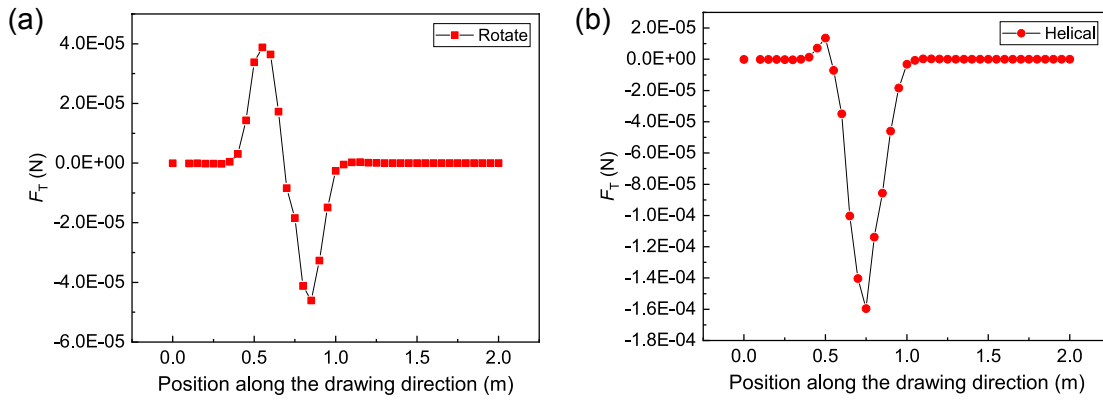
Fig. 5: F_T curves of the rotate (a) and helical (b) stirring (12 Hz and 43°) along the drawing direction (–)

The flow velocity distribution is displayed in Fig. 6. At first, under the condition of no drawing speed, in the region with higher flow velocity distribution, the direction of the vector in helical stirring is not only circumferential, but also along the length direction of casting billet [Fig. 6(a)]. Whereas for the rotate stirring, the flow velocity is almost uniformly distributed along the circumference [Fig. 6(b)]. As given in Figs. 6(c) and (d), both the flow velocity distribution in helical and rotate stirring under a specific drawing speed is composed of the flow zone in the center and the reverse flow region at its two sides along the drawing direction. Compared to rotate stirring, the maximum flow velocity along drawing direction in helical stirring is higher, indicating that the helical stirring can promote the flow of molten steel along drawing direction more sufficiently than rotate stirring.

Figures 7(a) and (b) reveal the temperature distribution of helical and rotate stirring. It is seen that both the isotherms are V-shaped, and the interval between adjacent isotherm in the two kinds of stirring are totally different. The interval between adjacent isotherm along drawing direction in helical stirring is shorter than the rotate stirring, and the length of the V-shaped isotherm is longer. This indicates that the temperature gradient along drawing direction in helical stirring is higher than the rotate stirring. Generally speaking, the higher temperature gradient along drawing direction is a favorable factor for the feeding capacity of billet.

The motion trajectory of tracer particles in helical and rotate stirring is plotted in Figs. 7(c) and (d). The calculation region is marked in Fig. 7(c), and the initial position of tracer particle is (0,0,0). The total length of calculation region is approximately 33.3% of the length of liquid cave. The length of the particle trajectory in the drawing direction during helical stirring is significantly longer compared to rotate stirring. This suggests that helical stirring is more effective in accelerating the flow of molten steel in three-dimensional directions.

The quantitative results of flow and temperature fields are shown in Fig. 8. It can be found the maximum flow velocity along the drawing direction inside the helical stirrer is 0.182 m·s⁻¹, which is obviously higher than that in rotate stirrer (0.127 m·s⁻¹) [Fig. 8(a)]. In addition, as shown in Fig. 8(b), the center-to-surface temperature difference in helical and rotate stirring are 3.6 °C and 4.3 °C, respectively. This indicates the helical stirring plays an important role in decreasing the radial temperature gradient of billet. The reduction in temperature gradient along radial direction is beneficial for the expansion of equiaxed crystal zone and the acceleration of simultaneous solidification [10].
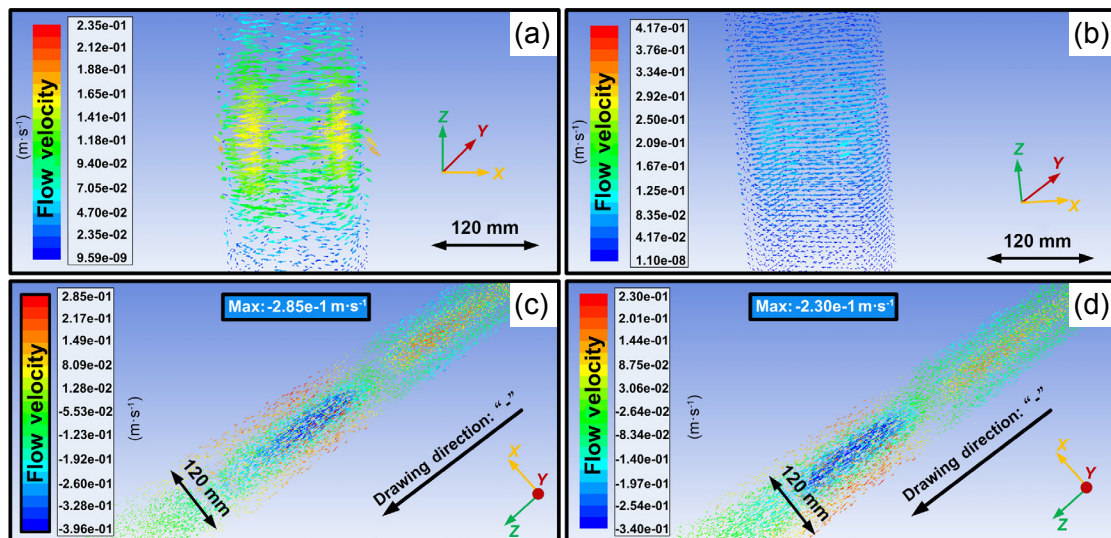

Fig. 6: Vector distribution of flow velocity under the condition of no drawing speed in helical (a) and rotate (b) stirring, and the corresponding distribution of flow velocity in the length direction (c, d)
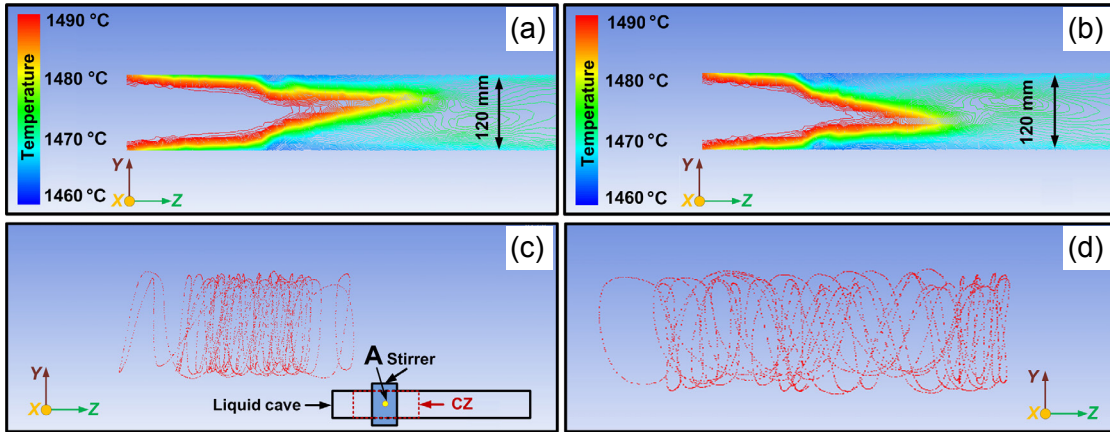
Fig. 7: Isotherm of rotate (a) and helical (b) stirring, and the tracer particle trajectory of rotate (c) and helical (d) stirring (CZ refers to calculation zone; A means initial position of tracer particles)
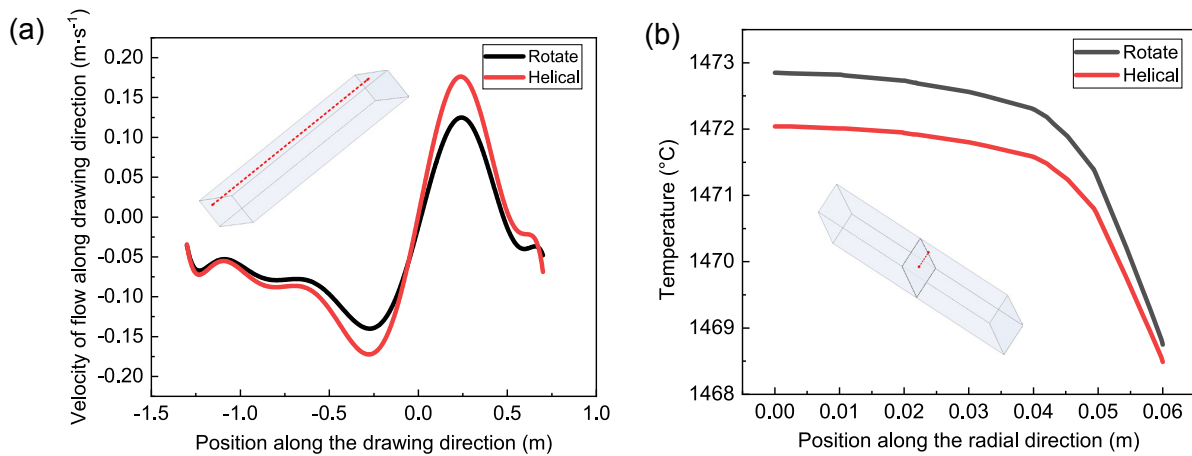

Fig. 8: Distribution curves of flow velocity in the drawing direction (a), and temperature distribution curve of the billet from center to surface (b)

In conclusion, helical stirring is superior in accelerating the flow of molten steel and reducing the temperature gradient along the radial direction of the billet. These factors contribute to facilitating simultaneous solidification and improving the quality of the billet.

It should be noted that the evolution trend of corresponding numerical simulation results of Al-8.8Si alloy is the same as that of 0.4%C-1.1%Mn steel in this study, so the results of numerical simulation of Al-8.8Si alloy will not be repeated here again.

4.3 Experimental validation and mechanism analysis

The magnetic stirring experiment was performed to make comparative analysis on stirring effect of helical and rotate stirring. The solidified macrostructures are presented in Figs. 9(a, b), and the distribution of Si content at different measuring points (the top, middle, and bottom) of Al-8.8Si alloy in both the two types of electromagnetic stirred samples is shown in Fig. 9(c). The measured Si content and the equiaxed ratio of the alloy are listed in Table 2. It is seen that the macrostructure of helical stirred sample is almost composed of equiaxed crystals, whereas, for rotate stirred sample, the content of columnar crystals is higher. The equiaxed ratio in helical stirred sample is 58.3% higher than that in rotate stirred sample. Furthermore,
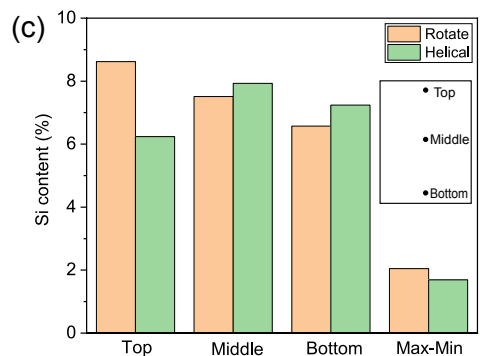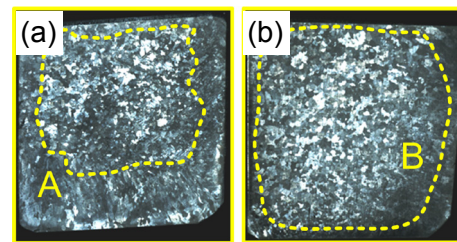

Fig. 9: Solidified macrostructures of Al-8%Si alloy under rotate (a) and helical (b) stirring, and histogram of Si content at different positions of the Al-8%Si ingot and its range (c) (stirring parameters: 43°, 75 A and 12 Hz); A–columnar crystal region, B–equiaxed crystal region

Table 2: Si content and equiaxed ratio of magnetic stirred Al-8%Si alloy

| Sample No.	Si content	
	Helical stirred	Rotate stirred
1	6.24%	8.62%
2	7.93%	7.51%
3	7.24%	6.57%
Range of Si content	1.69%	2.05%
Equiaxed ratio	95%	60%

the content range (the difference between the maximum and minimum values) of Si element in helical stirred sample is 17.5% lower than that in rotate stirred sample. Consequently, it can be inferred that the helical stirring has advantage in enhancing the equiaxed ratio and improving the element segregation of Al-8.8Si alloy.

Helical stirring shows a better effect on improving the quality of Al-8.8Si alloy ingot. To further verify the effectiveness of helical stirring, electromagnetic stirring experiments on 0.4%C-1.1%Mn steel were conducted. The longitudinal section of 0.4%C-1.1%Mn steel casting billet and in-situ detection results of element distribution (C, Mn) in the selected area of electric spark are shown in Fig. 10. The V-shaped shrinkage rate at the top of the helical stirred sample is lower than that of the rotary stirred sample [Figs. 10(a) and (b)], which is in accordance with the results of Figs. 7(a) and (b). The distribution of C and Mn element in helical stirred sample is also more homogeneous than that in rotate stirred sample. The segregation range of C/Mn in rotate and helical stirred sample are 0.2927/0.0701 (wt.%) and 0.2099/0.06 (wt.%), respectively. The statistical segregation coefficient (S) can be calculated based on the following equation:

$$S = \frac{\sqrt{\sum (C_i^2 - C_0^2)\big/ N}}{C_0} \tag{7}$$

where C_0 is the average carbon concentration, C_i is the carbon concentration of the ith detection point, and N is the number
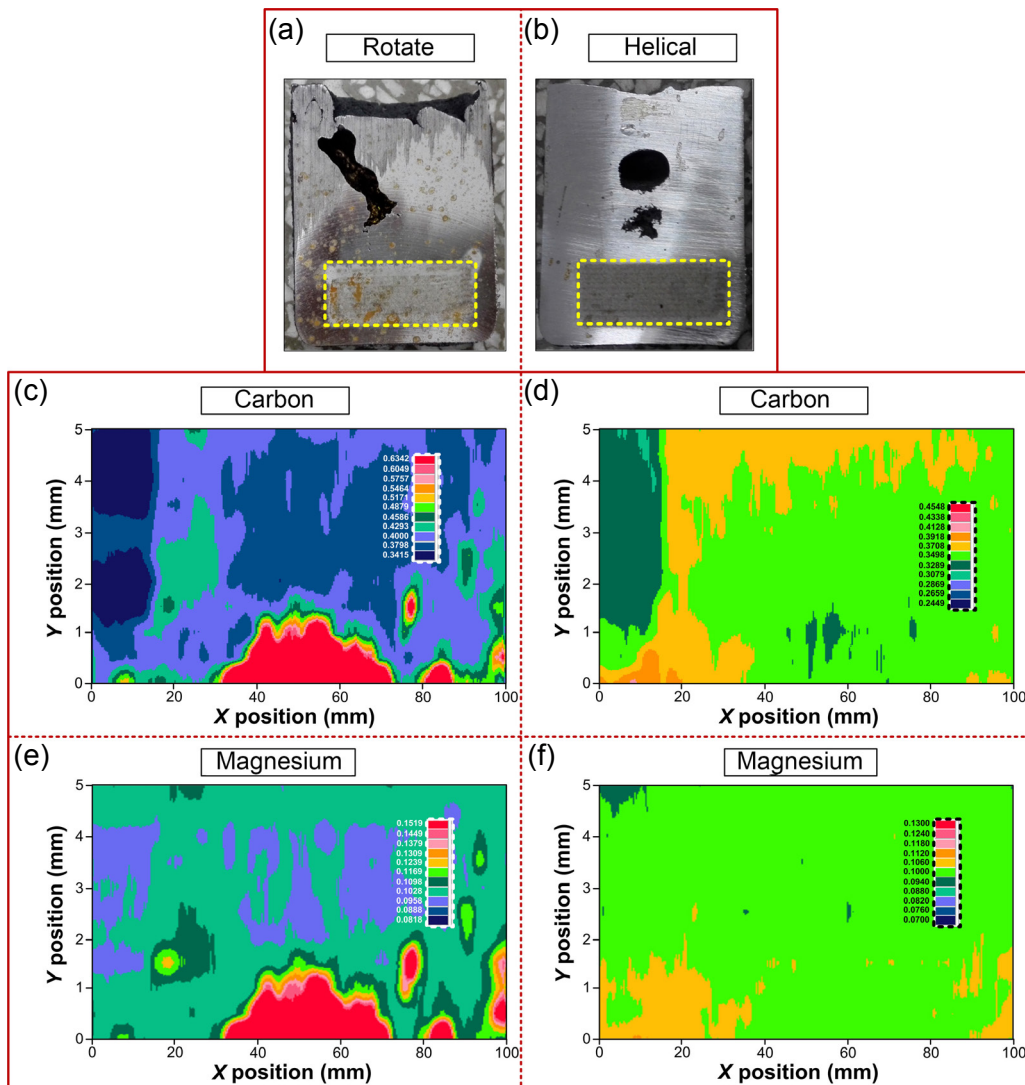
Fig. 10: 0.4%C-1.1%Mn steel casting billet (a, b), carbon distribution (c, d) and magnesium distribution (e, f) under rotate stirring (a, c, e) and helical stirring (b, d, f) (Stirring parameters: 300 A and 12 Hz)

of detection points. According to the statistics, the segregation coefficients of C in rotate and helical stirred sample are 0.0984 and 0.0876, respectively. In a word, the carbon segregation in helical stirred 0.4%C-1.1%Mn steel is reduced by 10.97%, compared with rotate stirred 0.4%C-1.1%Mn steel. Therein, the helical stirring is helpful to reducing element segregation of 0.4%C-1.1%Mn steel casting billet.

As mentioned above in Fig. 8, the radial temperature gradient ($\Delta T/\Delta x$, where ΔT is the temperature difference and Δx is the distance between adjacent isotherms) of helical stirred billet is lower than that of rotate stirred billet, and the movement speed (R) of solid-liquid interface is the fundamental reason for the above differences [15]. The relationship between $\Delta T/\Delta x$ and R is as follows [15]:

$$\begin{cases} \Delta d = \dfrac{K_1 \cdot d^{3/2}}{K_s^{1/2} \cdot \varepsilon^{1/2}(T_m - T_0) \cdot \delta_\Gamma} \cdot (\Delta T / \Delta x) \\ R \propto \Delta d \end{cases} \quad (8)$$

where Δd is the growth of dendrite size caused by temperature gradient, d refers to the dendrite size before growth, δ_Γ means the thickness of temperature boundary layer, ε represents interface mass transfer coefficient; T_m and T_0 are liquidus and environment temperature, respectively; K_1 and K_s are thermal conductivity of liquid and solid, respectively. According to Eq. (8), the decrease in temperature gradient can lead to the reduction of dendrite size, therefore, the movement speed of interface is also decreased.

The content of equiaxed crystals is related to the CET (columnar/equiaxed crystal transformation) coefficient. The interface movement speed also has significant influence on CET [16]:

$$\frac{(\Delta T / \Delta x)}{\sqrt{R}} \le \text{CET} \quad (9)$$

According to Eq. (9), it is evidenced that compared with temperature gradient, the movement speed of interface has greater effect on equiaxed crystal transformation. The lower the R, the earlier the equiaxed crystal transformation occurs, and thus, the equiaxed ratio is also increased.

The distribution coefficient of solute element (K_e) is regarded as the criterion of element segregation. The lower the K_e, the severer the element segregation [17]. The R is also a governed factor for K_e [17]:

$$K_e = \frac{K_0}{K_0 + (1 - K_0)\exp(-\dfrac{R}{D}\delta_\Gamma)} \quad (10)$$

where the K_0 is the value of K_e under equilibrium condition, D is diffusion coefficient of solute elements in liquid phase, and because the diffusion direction of solute elements in the liquid phase is opposite to the solidification direction, D has a minus value. According to Eq. (7), the smaller value of R can result in an increase in K_e. Therefore, the element segregation can be relieved via the control of interface movement.

Except for the decreased temperature gradient, the flow velocity induced by helical stirring is also critical to improving the billet quality. The solute elements enriched at the liquid cave will be stirred into the dendrite gap in a larger region under the effect of the helical electromagnetic force. Thereby, compared with rotate stirring, the center segregation of the billet will be more significantly eliminated by helical stirring. The influencing mechanism of helical and rotate stirring on equiaxed grain rate is depicted in Fig. 11. Generally, electromagnetic stirring force promotes the melting of delicate secondary dendritic arms, and then these free secondary dendritic arms will serve as heterogeneous nucleation nuclei to promote the expansion of equiaxed crystal regions. Compared with rotate stirring, the fused secondary dendrite arms under helical stirring will be carried to further distances by a higher flow velocity along the drawing direction, based on Figs. 7(c) and (d). As a result, the equiaxed ratio in helical stirred sample is increased.
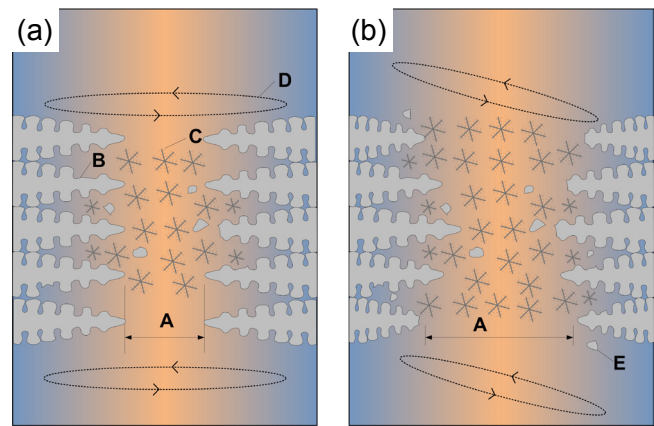

Fig. 11: Sketch maps showing the effect of electromagnetic force on expansion of equiaxed region: (a) rotate stirring; (b) helical stirring (A–width of equiaxed region; B–dendritic crystal; C–equiaxed crystal; D–electromagnetic force; E–free secondary dendritic arms)

To sum up, among these two electromagnetic stirring methods, the helical stirring can stimulate the flow of molten metal in all directions more substantially, which is conducive to the lower temperature gradient and simultaneous solidification. Subsequently, it is concluded that better billet quality can be obtained by helical electromagnetic stirring.

5 Conclusions

Numerical simulation and experimental analysis of rotate and helical electromagnetic stirring were carried out to make a systematic investigation for better quality amelioration of continuous casting billet. In view of the research data in this work, the following important conclusions are summarized:

(1) The magnetic yoke structure and stirring frequency of helical electromagnetic stirring have a significant impact on the stirring force in the drawing direction of the billet. The optimized stirring parameters are determined to be 43° and 12 Hz.

(2) The helical electromagnetic stirring can significantly increase the flow velocity and electromagnetic force in

drawing direction. In addition, the temperature gradient from the top to the bottom is also increased which is favorable for enhancing the feeding capacity. Moreover, the temperature gradient from the surface to the center is decreased so that the exquiaxed ratio can be increased.

(3) The billet quality can be better regulated by helical stirring. The equiaxed ratio of helical stirred Al-8%Si billet is 58.3% higher than the rotate stirred Al-8%Si billet. The element segregation values of Si in helical stirred Al-8%Si and C in helical stirred 0.4%C-1.1%Mn steel billet are reduced by 17.5 % and 10.97%, respectively, compared with rotate stirred samples.

Acknowledgments

Conflict of interest

The authors declare that they have no known competing financial interests or personal relationships that could have appeared to influence the work reported in this paper.

References

[1] Qiu Y, Zheng K H, Li X T, et al. Processing map of 2219 Al alloy prepared by internal electromagnetic stirring direct chill casting. Journal of Materials Research and Technology, 2022, 18: 2885−2895.

[2] Huang Y C, Wen J C, Zhao Y X. Effects of electromagnetic frequency on the microstructure and mechanical properties of $Al_{70}Zn_{10}Mg_{10}Cu_5Si_5$ medium entropy alloy. Journal of Materials Research and Technology, 2022, 17: 3105−3117.

[3] Han Z H, Wang Z M, Sun Z P, et al. Influence of non-uniform ultrasonic vibration on casting fluidity of liquid aluminum alloy. China Foundry, 2022, 19(5): 380−386.

[4] Pan D, Wang Y T, Guo Q T, et al. Grain refinement of Al-Mg-Si alloy without any mechanical deformation and matrix phase transformation via cyclic electro-pulsing treatment. Materials Science and Engineering: A, 2021, 807: 140916.

[5] Li Y F, Wang F L, Sun Q, et al. Study on the microstructure and impact toughness of TC11 titanium alloy by a novel electromagnetic shocking treatment. Materials Science and Engineering: A, 2023, 876: 145149.

[6] Zhang Y, Zhang W, Zeng L, et al. Segregation behavior and precipitated phases of super-austenitic stainless steel influenced by electromagnetic stirring. Materials Today Communications, 2022, 31: 103675.

[7] Zhang Z F, Li T J, Wen B, et al. Effect of multi-electromagnetic field on motion state at meniscus and quality of continuous casting metals. Journal of Iron and Steel Research, 2000, 12: 36−40.

[8] Zhao Q, Zhang X G, Zhang H Y, et al. Numerical simulation and experimental study on solidification process of Pb-Sn alloy under spiral magnetic field. Rare Materials and Engineering, 2014, 43(10): 2389−2394.

[9] Guo Q T, Wang T M, Jia J X, et al. Numerical study of flows driven by screw magnetic field in cylindrical container. International Journal of Cast Metals Research, 2013, 26: 92−99.

[10] Guo Q T, Tang X F, Li Z L, et al. Research on the influence of single winding helical electromagnetic stirring on the center segregation of high carbon large square billet. Materials Reports, 2022, 36(8): 21010147.

[11] Bridge M R, Rogers G D. Structural effects and band segregation formation during electromagnetic stirring. Metal Transaction B, 1984, 15(9): 581−587.

[12] Wang S B, Li J C. Numerical simulation of flow field and temperature field in continuous casting round billet under electromagnetic stirring. Foundry Technology, 2016, 37(4): 710−713. (In Chinese)

[13] Yang Z G, Wang B, Zhang X F, et al. Effect of electromagnetic stirring on molten steel flow and solidification in bloom mold. Journal of Iron and Steel Research (International), 2014, 21(12): 1095−1103.

[14] Guo Q T, Cao Z Q, Zhang Z T, et al. Separation efficiency of alumina particles in Al melt under high frequency magnetic field. Transactions of Nonferrous Metals Society of China, 2010, 10: 153−157.

[15] Duan M M, Chen C L, Li Z Y, et al. Effects of distribution of temperature and solute on the dendritic competitive growth. Special Casting & Nonferrous Alloys, 2009, 29(2): 126−129. (In Chinese)

[16] Bai L, Wang B, Zhong H G, et al. Experimental and numerical simulations of the solidification process in continuous casting of slab. Metals, 2016, 6(3): 53.

[17] Kurz W, Giovanola B, Trivedi R. Theory of microstruetural development during rapid solidification. Acta Metallurgica, 1986, 34(5): 823−830.